A new free-surface stabilization algorithm for geodynamical modelling: theory and numerical tests

Miguel Andrés-Martínez[a,*], Jason P. Morgan[a,**], Marta Pérez-Gussinyé[a,**], Lars Rüpke[b,**]

[a] Royal Holloway University of London, Earth Sciences, Egham, United Kingdom
[b] GEOMAR — Helmholtz Centre for Ocean Research, Kiel, Germany

Abstract

The surface of the solid Earth is effectively stress free in its subareal portions, and hydrostatic beneath the oceans. Unfortunately, this type of boundary condition is difficult to treat computationally, and for computational convenience, numerical models have often used simpler approximations that do not involve a normal stress-loaded, shear-stress free top surface that is free to move. Viscous flow models with a computational free surface typically confront stability problems when the time step is bigger than the viscous relaxation time. The small time step required for stability (< 2 Kyr) makes this type of model computationally intensive, so there remains a need to develop strategies that mitigate the stability problem by making larger (at least 10 $\sim$Kyr) time steps stable and accurate. Here we present a new free-surface stabilisation algorithm for finite element codes which solves the stability problem by adding to the Stokes formulation an intrinsic penalization term equivalent to a portion of the future load at the surface nodes. Our algorithm is straightforward to implement and can be used with both Eulerian or Lagrangian grids. It includes α and β parameters to respectively control both the vertical and the horizontal slope-dependent penalization terms, and uses Uzawa-like iterations to solve the resulting system

*Principal corresponding author
**Corresponding authors
Email addresses: miguel.andres-martinez.2011@live.rhul.ac.uk (Miguel Andrés-Martínez), jason.morgan@rhul.ac.uk (Jason P. Morgan), marta.perez-gussinye@rhul.ac.uk (Marta Pérez-Gussinyé), lruepke@geomar.de (Lars Rüpke)

at a cost comparable to a non-stress free surface formulation. Four tests were carried out in order to study the accuracy and the stability of the algorithm: 1) a decaying first-order sinusoidal topography test, 2) a decaying high-order sinusoidal topography test, 3) a Rayleigh-Taylor instability test, and 4) a steep-slope test. For these tests, we investigate which α and β parameters give the best results in terms of both accuracy and stability. We also compare the accuracy and the stability of our algorithm with a similar implicit approach recently developed by Kaus et al. (2010). We find that our algorithm is slightly more accurate and stable for steep slopes, and also conclude that, for longer time steps, the optimal α controlling factor for both approaches is ∼2/3, instead of the 1/2 Crank-Nicolson parameter inferred from a linearized accuracy analysis. This more-implicit value coincides with the velocity factor for a Galerkin time discretization applied to our penalization term using linear shape functions in time.
Keywords: free-surface stabilization, geodynamic modelling
2010 MSC: 00-01, 99-00

---

1. Introduction

Tectonics and mantle dynamics together with sedimentation and erosion build the Earth's surface topography (Anderson et al., 1973; McKenzie, 1977; Melosh and Raefsky, 1980; Hager et al., 1985; Willett, 1999; Beaumont et al., 2001; Koons, 2002; Finnegan et al., 2008; Braun, 2010). A topographical change translates into a change in the body forces governing the crustal and mantle dynamic processes. Additionally, there are feedbacks between surface erosion and topography (Ruddiman and Kutzbach, 1989; Braun, 2006) that make accurate topographic determinations desirable. The Earth's subaerial surface is a stress-free surface, which implies that both normal and shear stress should vanish at this interface (Harlow et al., 1965; De Bremaecker, 1976). Since surface and inner geodynamic processes are coupled, there is increasing interest in including stress-free surfaces and computationally similar submarine hydrostatic surfaces within geodynamic codes.

Several approaches to incorporate a free surface into geodynamical codes have been discussed during the last two decades. These include normal stress method, 'sticky-air' approaches, methods that treat the free surface as another variable of the flow problem, and a 'real' free surface. The normal-stress method remains most common because it is easiest to compute and also stable for time steps that are much larger than the viscous relaxation time of the system. It consists of an Eulerian top flat surface with free-slip boundary conditions for which stresses are calculated by solving the momentum equation, and where topography is post-calculated from normal stresses at the Eulerian surface nodes, by assuming that they are instantly compensated by the topographic load (McKenzie, 1977; Fleitout et al., 1986; Zhong et al., 1993, 1996). Although normal-stress methods are known to be computationally more efficient than real free surface ones, they are not able to solve the time-dependent relaxation of topography (Zhong et al., 1996; Crameri et al., 2012). If the relaxation time of a particular topographic wavelength is on the order of the time-scale of inner geodynamic processes, the relaxation of topography must also be considered. In this situation, a real free surface method is required to represent topographies that dynamically evolve with time (Zhong et al., 1996). The 'sticky-air' method consists of adding a low-viscous low-density layer at the top of the model, which is used as a proxy for air or water (Zaleski and Julien, 1990; Gerya and Yuen, 2003; Crameri et al., 2012), with the aim that the interface between the 'sticky-air' layer and the upper crust will behave similarly to a free surface. This method results into matrix singularities when the viscosity is too low, and introduces artefacts when the air/water layer is too viscous, because it can induce large stresses on the surface (Crameri et al., 2012). In practical use, any 'sticky-air' calculation should include post processing to determine that the sticky-air-to-surface interface is truly stress-free. Other methods treat the free surface as an additional independent variable and solve implicitly for it in conjunction with the Stokes equation (Kramer et al., 2012), or use implicit timestepping that has the nodal coordinates as part of the solution which can also yield a stable solution (Popov and Sobolev, 2008). Real free surface methods track the free surface in time and update it with the velocity calculated from solving the Stokes equation in the entire domain (Poliakov and Podladchikov, 1992). We chose to work with this method since it solves the time-dependent relaxation of topography and avoids artefacts associated with a 'sticky-air' layer without any additional calculation.

A stress-free surface, however, suffers from well-known instabilities when the time step is bigger than the viscous relaxation time (Zhong et al., 1996). Because the longest wavelength surface topography variations induce the most rapid rebound responses, we first consider the effects of surface topography with a wavelength of 1000 Km, to approximate the effects of a large-scale Plate Tectonics-related topographic variation in a given problem. For a relevant viscosity of 10^{21} Pa·s and surface density contrast of 2700 Kg/m^3, the viscous relaxation time of such a topographical feature would be of order $\sim$10 Kyr (Turcotte and Schubert, 1982). Thus, for time steps bigger than 10 Kyr topographic computations may become unstable. In Figure 1 it is shown why instabilities arise for time steps bigger than the relaxation time. In our example, the initial topography is a valley underlain by a constant viscosity fluid. In the presence of gravity, this topography should relax to a flat surface. In most geodynamic codes, the velocities at the nodes are calculated for the beginning of a time step and assumed constant through the whole step. However, if the time step is large compared to the viscous relaxation time, the velocities should decrease within the time step. Hence, a large time step leads to an overestimation of the velocity and topography at the end of the time step. In some cases, the final topography will be larger than the isostatically balanced topography and in the next time step the estimated velocity will be directed downwards and create a new 'valley artefact'. In the subsequent time step this valley will become again a positive topography (due to overestimation of the average velocity in the numerical time step) and so on. Hence, the topography will oscillate around the value for correctly compensated isostatic relief. This instability could occur not only at the beginning of a simulation in which case we could always run the model for small time steps and then switch to bigger time steps when stability is achieved, but could also occur for later stages of simulations that account for complex rheologies and/or geometries.

One of the most common free-surface instabilities that is observed at geodynamic codes is the so called 'drunken sailor' instability (Y. Podladchikov, personal communication, 2000). This instability occurs when the velocities for the surface are overestimated for a broad area on one part of the model, where in the opposite part the velocities are underestimated, and the resulting displacements overpass the isostatic equilibrium. Consequently, the topography of the previous step would be inverted. This phenomena could decay through a few time steps and then reach stability or, in case the overestimated velocities produce a displacement on the surface bigger than the initial topography, it will lead to the instability of the whole model.

Instabilities at a free surface will not occur for small enough time steps, since the new topography and the corresponding changes in body forces implied by it are included with sufficient accuracy in successive calculations. In our example, both the topography and upward velocity would be slowly reduced through the successive time steps leading to a stable solution (Fig. 1). Kramer et al. (2012) estimate that time steps to obtain a stable solution need to be at least one order of magnitude less than the time step in an identical simulation but employs a free-slip boundary. For simplistic viscous tests we have developed, $\sim$2000 year steps are small enough to prevent numerical instabilities for a layer with a viscosity of 10^{21} Pa·s. Although smaller time steps allow more accurate tracking of the topography, they are computationally expensive.

For this reason, it is desirable to develop algorithms that allow real free surface codes to run stable for relatively big time steps ($\geq$10 Kyr). Here, we present a new free-surface stabilisation algorithm (FSSA). It consists of adding a penalizing load to the real free surface, calculated implicitly from a fraction of the increment in height of the surface between the initial and the following steps. A similar FSSA algorithm was developed by Kaus et al. (2010). Their algorithm takes into account the surface traction terms derived from the time discretization of the momentum equations. Though their mathematical formulation is different, these terms also penalize the velocities as a function of the surface displacement along a time step in a similar way to our FSSA. Therefore, we have coded and tested both algorithms in order to check whether there are particular cases for which one algorithm gives a more accurate solution and/or allows a larger time step than the other while preserving stability. The results presented here were calculated with a modified version of MILAMIN (Dabrowski et al., 2008), which is a Lagrangian finite element method (FEM) solver for large 2D problems.

2. Methodology

Velocities and pressures are the unknowns of the mechanical problem in these geodynamic simulations. Velocities can be solved by using the Stokes equation for the viscous flow for incompressible flow:

$$\frac{\partial \tau_{ij}}{\partial x_j} - \frac{\partial P}{\partial x_i} = -\rho g_i, \tag{1}$$

where the deviatoric stress τ_{ij} can be written in terms of velocities in 2D, so for the x direction Stokes equation is:

$$\frac{\partial}{\partial x}\left[\eta\left(\frac{4}{3}\frac{\partial v_x}{\partial x} - \frac{2}{3}\frac{\partial v_y}{\partial y}\right)\right] + \frac{\partial}{\partial y}\left[\eta\left(\frac{\partial v_x}{\partial y} + \frac{\partial v_y}{\partial x}\right)\right] - \frac{\partial P}{\partial x} = -\rho g_x, \tag{2}$$

and for the y direction:

$$\frac{\partial}{\partial y}\left[\eta\left(\frac{4}{3}\frac{\partial v_y}{\partial y} - \frac{2}{3}\frac{\partial v_x}{\partial x}\right)\right] + \frac{\partial}{\partial x}\left[\eta\left(\frac{\partial v_x}{\partial y} + \frac{\partial v_y}{\partial x}\right)\right] - \frac{\partial P}{\partial y} = -\rho g_y, \tag{3}$$

where η is the viscosity, v_x and v_y are the velocities along the x and y directions respectively, P is the pressure, ρ is the density, and g_x and g_y are the accelerations along the x and y directions respectively (Dabrowski et al., 2008). The right-hand side of Eqs. 2 and 3 are the terms arising from the body force vector field. In this work we choose the positive y direction to be in the direction of the gravity vector, so that the acceleration g_x is 0 and g_y is Earth's gravity. In our code this is defined to be negative, so the horizontal body forces are zero and the vertical body forces are negative. Another equation is needed in order to solve for the pressure P. Using the relation between the mean stress changes and the volumetric strain rates we obtain:

$$\frac{\partial v_x}{\partial x} + \frac{\partial v_y}{\partial y} + \frac{P}{\kappa} = 0, \tag{4}$$

where κ is a 'penalty' volumetric viscosity coefficient analogous to the bulk modulus in linear elasticity (Hughes, 2000). For incompressible conditions $\frac{\partial v_x}{\partial x} + \frac{\partial v_y}{\partial y} = 0$. Therefore, $P\kappa^{-1} \approx 0$, so we assign κ a very big value ($10^6 \eta_{max}$) using it as a penalty factor (Hughes, 2000). We introduce a discretization for velocity and pressure into Eqs. 2, 3 and 4 using global shape functions N and Π, and we use the Galerkin method to derive the weak form. Then, we can rewrite this system of differential equations in the matrix form:

$$\begin{pmatrix} A & Q^T \\ Q & -\kappa^{-1} M \end{pmatrix} \begin{pmatrix} v \\ P \end{pmatrix} = \begin{pmatrix} F \\ 0 \end{pmatrix}, \tag{5}$$

where

$$A = \int_{\Omega^e} (\eta^e B^T D B) d\Omega, \tag{6}$$

$$Q = -\int_{\Omega^e} (\Pi B_{vol}) d\Omega, \tag{7}$$

$$M = \int_{\Omega^e} (\Pi \Pi^T) d\Omega, \tag{8}$$

$$B = \begin{pmatrix} \frac{\partial N_1}{\partial x}(x,y) & 0 & ... \\ 0 & \frac{\partial N_1}{\partial y}(x,y) & ... \\ \frac{\partial N_1}{\partial y}(x,y) & \frac{\partial N_1}{\partial x}(x,y) & ... \end{pmatrix}, \tag{9}$$

$$D = \begin{pmatrix} \frac{4}{3} & -\frac{2}{3} & 0 \\ -\frac{2}{3} & \frac{4}{3} & 0 \\ 0 & 0 & 1 \end{pmatrix}, \tag{10}$$

$$B_{vol} = \begin{pmatrix} \frac{\partial N_1}{\partial x}(x,y) & 0 & ... \\ 0 & \frac{\partial N_1}{\partial y}(x,y) ... & \end{pmatrix}, \tag{11}$$

$$F = \int_{\Omega^e} (\rho g) d\Omega, \tag{12}$$

where η^e is the viscosity over the element, B defines the FE strain rate matrix, $\eta^e D$ is the constitutive tensor in Voigt notation, v and P are the velocity and pressure unknowns, F contains the body forces per volume and the boundary integrals over all forces acting on the modelling domain Ω with boundaries S, and Ω^e is an element domain (Hughes, 2000). It is possible to formally solve for pressure $P = \kappa M^{-1} Q v$ and then simplify this system of equations to equations only for vector v:

$$Kv = F, \tag{13}$$

where $K \equiv A + \kappa Q^T M^{-1} Q$ is the penalized stiffness matrix for incompressible flow (Hughes, 2000; Zienkiewicz et al., 1985). Here, we use Crouzeix-Raviart triangular elements with quadratic velocity shape functions enhanced by a cubic bubble function and discontinuous linear interpolation pressure (Crouzeix and Raviart, 1973). Meshes were generated employing the Triangle Mesh Generator developed by Shewchuk, J. R. (Shewchuk, 1996; http://www.cs.cmu.edu/∼quake/triangle.html, version 1.6, 2005).

2.1. Free-surface approach

For a surface node at the beginning of a time step n, we can define an increment to the surface height Δh_{n+1} for this node. We assume that the x-location of this interpolation for h_{n+1} is fixed to the current x-location for each surface node. In this case, the topographic change during this time step is given by:

$$\Delta h_{n+1} = \Delta h^x_{n+1} + \Delta h^y_{n+1}, \tag{14}$$

$$\Delta h_{n+1} = -\delta t \left(\frac{\delta \bar{h}}{\delta x} \right) v_x + \delta t v_y, \tag{15}$$

where δt is the time step, v_x and v_y are the time-averaged x- and y-velocity components calculated at this node along top surface, and $\left(\frac{\delta \bar{h}}{\delta x}\right)$ is an approximation to the slope of the top surface during the time step (Fig. 2). The negative sign of the horizontal term is needed to determine the change in relief due to positive (rightwards) advection of a positive (up to the right) slope (Fig. 3a, b, c and d).

To stabilise the displacement calculated with a large time step, we chose to damp the velocity solution by adding, during that time step, a portion of the load that would correspond to a fraction of the estimated displacement Δh_{n+1}. At the end of the time step this can be expressed as:

$$\Delta \bar{h}_n = \alpha \left(-\beta \delta t \left(\frac{\delta \bar{h}}{\delta x} \right) v_x + \delta t v_y \right), \tag{16}$$

where α is a number between 0 and 1 to control what fraction of v_x and v_y contribute to $\Delta \bar{h}_n$, and β is also a number between 0 and 1 to control the contribution of v_x alone. The force produced by the load $\Delta \bar{h}_n$ is:

$$F_{FS} = -\int_S \rho g_y \alpha \beta \delta t \left(\frac{\delta \bar{h}}{\delta x} \right) v_x dx + \int_S \rho g_y \alpha \delta t v_y dx. \tag{17}$$

where ρ is the density of the rock for the subareal case, or density contrast between the rock and the water for the submarine case, and g_y is gravity. Here we assume that the slope is relatively constant along the time step, so $\left(\frac{\delta \bar{h}}{\delta x}\right) \approx \left(\frac{\delta h}{\delta x}\right)_n$. Separating the x and y terms of the F_{FS} and incorporating this force into the standard weak formulation (Hughes, 2000, p. 25):

$$F_{FS}^{yx}{}_i = -\rho g_y \alpha \beta \delta t \left(\frac{\delta h}{\delta x}\right)_n \int_S N_i N_j v_{xj} dS, \tag{18}$$

$$F_{FS}^{yy}{}_i = \rho g_y \alpha \delta t \int_S N_i N_j v_{yj} dS, \tag{19}$$

where F_{FS}^{yx} and F_{FS}^{yy} are the different terms of the force along the y axes (first superscript) due to the displacements along the x and y axis (second superscript) respectively, i is the global index of all nodes at the free surface, and N are the shape functions evaluated along the surface. Note that these penalization forces will always work in the opposite sense of the surface displacement since the gravity g is defined to be negative (Fig. 3). In order to stabilise the free surface we add both forces into the right hand side of Eq. 13, which is equivalent to add the average load due to $\Delta \bar{h}_n$ over the time step:

$$Kv = F + F_{FS}^{yx} + F_{FS}^{yy}. \tag{20}$$

Since F_{FS}^{yx} and F_{FS}^{yy} are expressed in weak formulation it is possible to write:

$$Kv = F + K_{FS}^{x} v_x + K_{FS}^{y} v_y, \tag{21}$$

where K_{FS}^{x} and K_{FS}^{y} are stiffness-shape terms which include ρ, g_y, the parameters α and β, and the shape functions N. We can therefore rewrite the Eq. 21 as:

$$[K - K_{FS}^{x} - K_{FS}^{y}]v = F. \tag{22}$$

The system of Eq. 22 is now solved for the velocities (and pressures) which leads to a more stable and accurate solution for the velocities along the free surface. Note that we are using the vertical and horizontal velocities of each surface node to calculate the future vertical displacement at the current horizontal location of the node for the topographic variation during the time step (Fig. 2). Therefore, this is an Eulerian formulation. This is justified because the correction is applied at the node location as the solver is used for this configuration of the mesh. Also note that although we developed this formulation for the top surface where the largest density contrast is expected, it can also be applied to any internal interface across which there is a density contrast.

In order to implement the proposed algorithm into a FEM code, it is necessary to build the K^x_{FS} and K^y_{FS} matrices. These additional matrices incorporate typical forms in the usual stiffness matrix K. Here we show a 2D example of the stiffness-matrix structure for an element K_e:

$$K_e = \begin{pmatrix} k^{xx}_{11} & k^{xy}_{11} & k^{xx}_{12} & k^{xy}_{12} & . & . & k^{xx}_{1n} & k^{xy}_{1n} \\ k^{yx}_{11} & k^{yy}_{11} & k^{yx}_{12} & k^{yy}_{12} & . & . & k^{yx}_{1n} & k^{yy}_{1n} \\ k^{xx}_{21} & k^{xy}_{21} & k^{xx}_{22} & k^{xy}_{22} & . & . & k^{xx}_{2n} & k^{xy}_{2n} \\ k^{yx}_{21} & k^{yy}_{21} & k^{yx}_{22} & k^{yy}_{22} & . & . & k^{yx}_{2n} & k^{yy}_{2n} \\ . & . & . & . & k^{xx}_{ij} & k^{xy}_{ij} & . & . \\ . & . & . & . & k^{yx}_{ij} & k^{yy}_{ij} & . & . \\ k^{xx}_{n1} & k^{xy}_{n1} & k^{xx}_{n2} & k^{xy}_{n2} & . & . & k^{xx}_{nn} & k^{xy}_{nn} \\ k^{yx}_{n1} & k^{yy}_{n1} & k^{yx}_{n2} & k^{yy}_{n2} & . & . & k^{yx}_{nn} & k^{yy}_{nn}, \end{pmatrix} \tag{23}$$

where n is the number of nodes in the element. The first superscript of k indicates the direction of the force resulting from multiplying k by its respective v in Eq. 13. The second superscript indicates the direction of the velocity v which is multiplying k, and the subscripts i and j indicates the shape functions involved in the calculation of the component. Our penalizing force F_{FS} has both F^{yx}_{FS} and F^{yy}_{FS} components that are applied in the y direction, and are calculated from the velocities v_x and v_y at the surface nodes. Therefore, K^x_{FS} and K^y_{FS} matrices will be 0 everywhere, except for the components $k^{yx}_{FS ij}$ and $k^{yy}_{FS ij}$ at surface nodes:

$$k^{yx}_{FS ij} = -\rho g_y \alpha\beta\delta t \left(\frac{\delta h}{\delta x}\right)_n \int_S N_i N_j dS, \tag{24}$$

$$k^{yy}_{FS ij} = \rho g_y \alpha\delta t \int_S N_i N_j dS. \tag{25}$$

The annexe includes an example of coded $k^{yx}_{FS ij}$ and $k^{yy}_{FS ij}$ for a 2D FEM model.

The stiffness matrix for a flow solver is typically symmetric so it is possible to apply the computationally efficient Cholesky decomposition method to solve it. The matrix K^y_{FS} is also symmetric, so that subtracting it from the stiffness matrix would have little effect on computing time. However, K^x_{FS} is not symmetric, since its non-zero values are located off-diagonal in the lower-triangular matrix (Eq. 23), so subtracting it from the stiffness matrix would make a symmetric Cholesky decomposition impossible. LU decomposition could be applied in this case, but this would considerably degrade the performance of the code. We have chosen to use an iterative operator split into symmetric and asymmetric matrices that can use Cholesky decomposition for inversion of a symmetric matrix with multiple back-substitutions. This approach is ∼100 times faster than a full LU decomposition for the resolution used in our experiments (10-30 Km). In this iterative solution the symmetric matrix K^y_{FS} is subtracted from the stiffness matrix, then Cholesky factorization is applied to this matrix. The system of equations is solved in which the right hand-side of the system consist of the body forces F plus our correcting free surface force term F^{yx}_{FS} or $K^x_{FS} v_{it-1}$:

$$[K - K^y_{FS}] v_{it} = F + K^x_{FS} v_{it-1}, \tag{26}$$

where it is the number of the current iterative approximation to the solution at this time step. The first iteration v_{it-1} is assumed to be 0, so F^{yx}_{FS} is also 0. In each new iteration v_{it-1} is updated using the velocities calculated in the previous iteration. The loop runs until the solution converges. Typically, FEM codes for a incompressible flow also use an 'Uzawa' iterative solution algorithm in order to achieve incompressibility. Here, 'Uzawa' is the name used by Zienkiewicz et al., 1985 to describe their proposed 'iterative improvement' of a penalty formulation for incompressible flow. Other geodynamics papers use the overused term 'Uzawa' to mean different, but related, numerical algorithms. We merge both iterations by applying two loops, an outer loop which updates the velocities from the previous iteration and adds $K^x_{FS} v_{it-1}$ to the right-hand side

Rhs of the Eq. 13, and an inner loop which iterates to obtain incompressibility:

$Loop1\ it = 1 : m$

Operator split, asymmetric matrix terms moved to Rhs:

$Rhs = F + K^x_{FS} v_{it-1}$

Zienkiewicz et al., 1985 'Uzawa iteration':

$Loop2\ uz = 1 : n$

$u = [K - K^y_{FS}]^{-1} Rhs$

$Div = Q' M^{-1}$

$Rhs = Rhs - \kappa Div Q$

end

end

where m and n are the number of iterations for each loop, Div is the divergence, κ is the pressure-formulation penalty factor, and Q and M are the parts of the stiffness matrix indicated in Eqs. 7 and 8 respectively. Note that the matrix $K - K^y_{FS}$ is formed and Cholesky-factorized only once per time step so that all Rhs and incompressibility-preserving subiterations only involved relatively cheap and fast Cholesky back-substitutions analogous to the back-substitutions in a typical Uzawa algorithm for incompressibility.

3. Results

Four experiments were conducted in order to test the stability and the accuracy of the above algorithm and also to explore which α and β parameters are 'best' for practical use. These experiments exhibit both 'drunken sailor' instabilities and/or meshing problems when the time step is too large. The experiments are: a) a decaying first-order sinusoidal topography test, b) a decaying high-order sinusoidal topography test, c) a Rayleigh-Taylor instability test, and d) a steep-slope test. The test for the topography of a half-sinusoidal initial relief consists of a single layer experiment with constant viscosity and an initial top-surface relief imposed as a half-sinusoid. Theoretically, this topography should evolve towards a flat surface. This experiment is appropriate for testing the stability and the accuracy of our algorithm since it introduces the longest wavelength, highest amplitude form of the 'drunken sailor' instability. For time steps >14 Kyr for the given 10^{21} Pa·s viscosity this instability occurs for a simple free surface. The 50th-harmonic test is a variation of the previous test but with a much shorter wavelength sinusoidal topography. For this topographic variation the predicted relaxation time is bigger (Turcotte and Schubert, 1982). However, this test is convenient since it allows us to check the accuracy of our FSSA for steep-slopes and its ability to reduce the numerical artefact involving a self-intersecting top surface (Fig. 4). The Rayleigh-Taylor instability test is a two-layer viscous flow experiment, in which the upper layer is more viscous and denser than the lower layer, resulting in a Rayleigh-Taylor instability beneath the free surface. The instability is triggered by relief on the interface between the two layers, which helps the upper layer to start sinking where it is thicker, and the lower layer to start rising where the upper layer is thinner. The solution of the Rayleigh-Taylor instability is highly sensitive to the top-surface topography, so that a badly constrained free surface also induces the 'drunken sailor' instability which does not allow the Rayleigh-Taylor instability to evolve properly. Finally, the steep-slope test is a single-layer viscous experiment that has a steep slope in its initial topography. Theoretically the slope should become smoother through time and finally become a stable flat top surface. Although this experiment does not lead to a drunken-sailor type instability, the horizontal component of the velocity affects the slope of the top surface so it is a suitable experiment to better evaluate the effects of the K^x_{fs} correction terms. Table 1 summarizes the parameters used in the different experiments.

In order to investigate the accuracy of our algorithm, we compare the experiments to a reference solution determined for a very small time step of 100 yr and a 'simple' free surface. Based on the tests we made for solutions run with small 100 yr and 200 yr time steps (see Table 2), the reference solution appears likely to be better than 1×10^{-2} m accuracy (RMS error) for all tests, and that we chose to use $\alpha = 0$ for the reference solution so that we would not use a FSSA for the reference solution. We next discuss the accuracy comparing the topographies generated with the FSSA tests with this reference solution. We found it also necessary to determine the biggest stable time step for the non-FSSA approach, since it defines for which δt the tests become unstable without FSSA, and is useful as a reference when discussing the improved stability of the FSSA approaches.

3.1. Decaying-half-sinusoidal test

Decaying-half-sinusoid tests with $\alpha = 1$, 0.75, 0.7, 2/3, 0.6, 0.5 and 0.25, and $\beta = 1$ and 0, were run for time steps $\delta t = 0.5$, 1, 2, 2.5, 4, 5, 10 and 20 Kyr. These results show that introducing the penalization for the horizontal component of the velocity K^x_{fs} ($\beta = 1$) produces almost the same surface relief as the computationally faster tests that just include the vertical penalization K^y_{fs} (*e.g.* $\beta = 0$). The experiment starts to become unstable without FSSA for δt>14 Kyr. For small time steps (< 5 Kyr) $\alpha = 0.5$ yields the most accurate results, while $\alpha = 0.7$, 2/3 and 0.6 give the most accurate results for FSSA approach with $\delta t \geq 20$ Kyr (Figs. 5 and 6).

3.2. Decaying 50th-harmonic-sinusoidal relief test

This test was run for $\delta t = 10$, 20, 50, 100 and 400 Kyr, for $\alpha = 1$, 0.75, 0.7, 2/3, 0.6, 0.5 and 0.25, and for $\beta = 1$ and 0. The highest accuracy was achieved for $\alpha = 0.25$ and 0.5 for the smallest time steps, and for $\alpha = 0.7$, 2/3 and 0.6 for $\delta t = 400$ Kyr (Fig. 7a and b). Root-mean-square errors (RMS) show that using $\beta = 0$ gives results that are slightly more accurate than $\beta = 1$ for these tests.

3.3. Rayleigh-Taylor instability test

Rayleigh-Taylor instability tests with $\alpha = 1$, 0.75, 0.7, 2/3, 0.6, 0.5 and 0.25, and $\beta = 1$ and 0 for $\delta t = 10$ and 20 Kyr, show similar results to that of decaying-sinusoidal surface topography. Both $\delta t = 10$ and 20 Kyr lead to an instability without FSSA stabilization. Even with FSSA, the free surface becomes unstable for $\alpha = 0.25$ when $\delta t = 10$ Kyr, and for $\alpha = 0.25$ and 0.5 when $\delta t = 20$ Kyr. Again, results indicate a better accuracy for a 10 Kyr time step with $\alpha = 0.5$, while $\alpha = 0.6$ produces the most accurate results followed by $\alpha = 2/3$ (Fig. 7c and d) for larger time steps. Topographies calculated with $\beta = 0$ and 1 do not differ significantly from each other. The RMS error with respect to the 100 yr non-FSSA reference solution shows that the calculations done with $\beta = 0$ are again slightly more accurate than those calculated with $\beta = 1$ (Fig. 7c and d).

3.4. Steep-slope test

The steep-slope test has been run for $\delta t = 20$ Kyr with $\alpha = 1$, 0.75, 0.7, 2/3, 0.6, 0.5 and 0.25 and $\beta = 1$ and 0. Calculations done with $\alpha = 0.5$, 0.6 and 2/3 result in the most accurate outcomes (Fig. 8a). Fig. 7e shows that $\alpha = 2/3$ gives better results after 6 Myr, whereas $\beta = 0$ gives the most accurate results for the first 12 Myr while $\beta = 1$ gives the most accurate results after 14 Myr of surface evolution.

4. Discussion

As mentioned above, our formulation differs conceptually from that previously presented by Kaus et al. (2010). They also applied an implicit penalizing load to the stiffness matrix, but did this using the surface traction terms derived from the time discretization of the momentum equation, which translated into using a normal-to-the-surface velocity vector ($v_x n_x$, $v_y n_y$) instead of out 'Eulerian' approach using velocity directions at the node (Fig. 2). Their equivalent penalizing terms ${k_K^{yx}}_{ij}$ and ${k_K^{yy}}_{ij}$ can be defined as:

$$ {k_K^{yx}}_{ij} = n_x \rho g \alpha_K \delta t \int_S N_i N_j dS, \tag{27} $$

$$ {k_K^{yy}}_{ij} = n_y \rho g \alpha_K \delta t \int_S N_i N_j dS, \tag{28} $$

where α_K is their FSSA controlling factor, for which they showed 0.5 is the optimal value among 0, 0.5 and 1 (Kaus et al., 2010). Their algorithm is formulated to be applied at every element boundary, while we apply it only at the free surface. Their penalization terms cancel out between elements of equal densities, so the penalization is only effective at the free surface or at interfaces where changes in density occur. This results in better estimates for multilayer models even if free slip is imposed at the surface. Since only one of our tests was multilayered, we chose to apply the stabilization algorithm only at the surface, but it too would be easy to implement at internal density interfaces, but not as a general correction for all elements. Assuming that the slope of the surface can be defined as $\frac{\partial h}{\partial x} = -\frac{n_x}{n_y}$, then their formulation is equivalent to ours (Eqs. 24 and 25) multiplied by n_y. In order to improve the performance of their algorithm, they assumed $n_x \approx 0$, as is true for small slopes. In this case, ${k_K^{yx}}_{ij} = 0$ and the resulting penalized stiffness matrix is symmetric. However, processes that typically transform topography, such as erosion and faulting, can produce steep-enough slopes for models to require the horizontal term to increase numerical stability.

We also included Kaus et al., 2010 FSSA into our tests for comparison, and to test for the 'best practice' values for α_K. We ran the same tests as for our FSSA, with $\alpha_K = 1$, 0.75, 0.7, 2/3, 0.6, 0.5 and 0.25. The results show that $\alpha_K = 0.5$ produces the most accurate solutions for smaller time steps, while $\alpha_K = 1$ produces the most stable solutions, as suggested by Kaus et al. (2010). However, for the decaying-sinusoidal topography and Rayleigh-Taylor tests, we find that $\alpha = 0.6$ and 2/3 are the best for accuracy with their approach when using time steps bigger than the maximum stable time step for a non-FSSA approach. Except for the steep-slope test (Fig. 7e) where our algorithm produces slightly more accurate results for the $\delta t = 20$ Kyr test after 14 Myr of time-run for $\alpha = 2/3$ and both $\beta = 1$ and 0 (being $\beta = 1$ results the most accurate), there are no major differences between the results produced with the Kaus et al. (2010) FSSA and our FSSA in accuracy.

Based on the results of these tests, we suggest that for large FSSA-stabilized time steps, one should use $\alpha = 2/3$ for 'best practice' results (best accuracy and stability together) for both our and Kaus et al. (2010) algorithms. Note that a 2/3 value would be obtained for a standard finite-element Galerkin discretization in time with linear shape functions in time, as opposed to a standard finite-difference approximation in time that is normally used. The finite-element-like Galerkin time-discretization results in a factor of 2/3 that multiplies the unknown at the end of the time step, while the factor obtained from a finite-difference Crank-Nicolson formulation (less stable but theoretically more accurate at smaller time steps) is 1/2. Applying a Galerkin discretization in time using linear shape functions $M(t)$ in Eq. 20, following the scheme described in Warzee (1974), one obtains:

$$\int_{time} M_s[K \sum_{u=0}^{r} M_v v_u - \delta t A \sum_{u=0}^{r} M_u v_u - F(t)]dt = 0, \tag{29}$$

where $\delta t A \sum M_u v_u$ is equivalent to the penalization term F_{FS}, $A_{ij} = -\rho g \left(\frac{\delta h}{\delta x}\right) \int_S N_i N_j dS$ for the horizontal penalization term, and $A_{ij} = \rho g \int_S N_i N_j dx$ for the vertical penalization term. Integrating through a time step δt:

$$K\left(\frac{1}{3}u_0 + \frac{2}{3}u_1\right) - \delta t A\left(\frac{1}{3}v_0 + \frac{2}{3}v_1\right) - \left(\frac{1}{3}F_0 + \frac{2}{3}F_1\right) = 0, \tag{30}$$

where the subindexes 0 and 1 indicate whether the variables are calculated for the beginning or the end of the time step, respectively. Therefore, 2/3 would also be the parameter for the Galerkin time discretization of our stabilization term, coinciding with the 'best practice' α found in our numerical tests.

Results often show worse RMS errors with the penalized horizontal stabilization term ($\beta = 1$) than without it ($\beta = 0$) (Fig. 7). This can be anticipated since $\beta = 1$ introduces an additional load at the top of the surface (as well as $\alpha > 0$), which for cases where the time step is small and/or the surface is stable implies that the error could be increased in the calculations as a byproduct of greater stability. However, for $\alpha = 2/3$, $\beta = 1$ gives smaller RMS at the last stages of the multiple harmonics test with $\delta t = 400$ Kyr (Fig. 7b), and the last stages of the steep-slope test for $\delta t = 20$ Kyr (Fig. 7e). This two tests produce the highest surface horizontal displacements from the set of tests we run and, therefore we conclude that, for near-optimal α, $\beta = 1$ can improve the accuracy of models that have a tendency for lateral instability.

In order to study stability of the different FSSAs these tests were pushed to values of δt for which they become numerically unstable with $\alpha = \alpha_K = 0.5$ and 2/3 (Table 3). Results show that both our and the Kaus et al. (2010) algorithms can be used for a time step at least 2 times bigger than the maximum for a non-FSSA test for the worst-case decaying half-sinusoid and steep-slope tests, and at least one order of magnitude more than the non-FSSA for the other situations. $\alpha = \alpha_K = 2/3$ allows bigger time steps than $\alpha = \alpha_K = 0.5$, except for the 50th-harmonic sinusoid test. There are no major differences in the maximum time step, independent of the FSSA or choice of β parameter for the decaying-half-sinusoid and Rayleigh-Taylor instability tests. However, the Kaus et al. (2010) FSSA allows a slightly bigger time step (570 Kyr in contrast to 510 Kyr) for the decaying 50th-harmonic sinusoid test for $\alpha = 2/3$, without inducing a self-intersecting surface artefacts, while our FSSA results into the maximum time step without meshing problems (5.9 Myr in contrast to 5.6 Myr) for $\beta = 0.5$, and the worse results (4.3 Myr) for $\beta = 1$.

In order to solve the asymmetric system our FSSA combines Cholesky factorization with Uzawa-like iterations, as previously explained. In order to converge, the FSSA with the vertical and horizontal penalty terms needs $\sim$5 times more 'backsolve' operations than the vertical-only penalized form. We expect that for different resolutions than the ones used here, and even for 3D, the number of backsolve operations needed for convergence would vary little for similar viscosities since the convergence of Uzawa-like iterations only weakly depends on the number of unknowns (Zienkiewicz et al., 1985). Consequently, the solver for the asymmetric system is spending approximately 5 times more 'backsolve' operations than the one for the symmetric system. However, the performance is still good in contrast with a solver that applies LU factorization, since LU can spend more than 100 times the computing-time (for the given resolution) than the forward Cholesky factorization, which is the most time-intensive portion of the Cholesky forward-backsolve solution process.

The algorithm presented here is formulated and tested for finite element discretization. However, many experiments within the modelling community are done with staggered finite difference codes. These models also suffer from free surface instabilities (Duretz et al., 2011), so a free-surface stabilization algorithm is also required. A generalized formulation of our FSSA is obtained by applying a body force penalization term to Eqn. 1 at the surface (and/or density interfaces) cells:

$$\frac{\partial \tau_{ij}}{\partial x_j} - \frac{\partial P}{\partial x_i} = -\rho g_i + F_{FS}, \tag{31}$$

where

$$F_{FS} = \frac{\delta \rho}{\delta y} g_y \alpha \delta t \left(-\beta \frac{\delta \bar{h}}{\delta x} v_x + v_y \right), \tag{32}$$

where $\frac{\delta \rho}{\delta y}$ is the vertical density change across the free surface or density interface. This generalized formulation of our FSSA can be implemented in finite difference codes.

Here, we have demonstrated that: 1) the damping factor $\alpha = 2/3$ works best in the limit of maximum stable time steps both for Kaus et al., 2010 and our FSSAs, and 2) the horizontal term of the stabilization algorithm is not necessary for steep slopes (up to 30°), meaning that Kaus et al., 2010 approach, where the horizontal term is neglected, is a good approach since it still makes little practical difference to include the horizontal term for extreme topographies. We also present an operator-split method for implementing the horizontal term that retains symmetric stiffness matrix, in case readers do wish to economically use this approach for very steep slopes. Future work to be addressed in a follow-up paper would include: 1) a more exhaustive examination of the relative performance (CPU time versus accuracy and stability) of proposed free-surface stabilization algorithms; 2) a study of the stability radius for the semi-implicit time integrators; and 3) comparison with additional methods of free surface stabilization such as the implicit algorithm proposed by Kramer et al., 2012 or methods in which the surface is updated during every strain iteration of a non-Newtonian solution so that instabilities are mitigated without need for an explicit stabilization algorithm (i.e. Popov and Sobolev, 2008).

5. Conclusions

Numerical flow models with free surfaces need a free-surface stabilisation algorithm (FSSA) in order to be stable at relatively large time steps ($\geq$10 Kyr) that allow for a reasonably small compute time. We have developed a FSSA algorithm which adds to the mechanical system a load calculated implicitly from a portion of the difference in surface relief between the beginning and end of a time step. This FSSA allows time steps 2-20 times larger than the free surface models without stabilization, and produces accurate results ($< 1\%$ relative error) for the viscosities and time steps used in these tests. The magnitude of the additional implicit surface load during a time step is controlled by parameters α and β, where α corresponds to the total controlling factor of the load (with values between 0 and 1), which β controls only the horizontal term of the load (with values also between 0 and 1). In addition, we have implemented an Uzawa-like iteration in this algorithm that allows us to solve the asymmetric system resulting from $\beta = 1$ in compute time comparable to that for the symmetric solution with $\beta = 0$.

Different viscous experiments were carried out in order to numerically assess the 'best-practice' values for α and β. For time steps close to the stability limit for models without a FSSA, $\alpha = 0.5$ results in the most accurate free surface approximation, while for time steps larger than those stable in models without a

FSSA, $\alpha = 2/3$ is found to be the best option for both our FSSA and the FSSA described by Kaus et al. (2010), because it generally yields the most accurate and stable results.

Including the horizontal term in our FSSA ($\beta = 1$) gives generally slightly less accurate results than omitting it ($\beta = 0$), except for the steep-slope test after several million years. The maximum time steps achieved with stability for our and the Kaus et al. (2010) FSSAs are very similar for all tests explored here. Although the multiple-harmonic topography test and the steep-slope test never become unstable before they experience mesh-deformation-related problems in our Lagrangian tests, the Kaus et al. (2010) algorithm allows slightly bigger time steps without mesh-deformation-related problems for the 50th-harmonic-sinusoidal relief test, while our algorithm with $\beta = 0.5$ allows the use of slightly larger time steps for the steep-slope test. Although our FSSA with $\beta = 1$ should intuitively give more stable results for steep slopes than the FSSAs without the horizontal stabilization term, as it is, in theory, a more complete approximation, our tests did not demonstrate a significant improvement over FSSA approximations with $\beta = 0$. We did see that it leads to more accurate results for the latest stages of the relaxation of a initial steep-slope, with only a minor increase in computational time with respect to FSSA methods that neglect this additional term. Our final recommendation: use FSSA, with $\alpha = 2/3$.

Acknowledgments

We would like to acknowledge Dave May and Boris Kaus for very exhaustive and constructive reviews, which have greatly improved the quality of this manuscript. We also thank Royal Holloway University for supporting this research through a Reid Scholarship.

References

Anderson, R.N., McKenzie, D., Sclater, J.G., 1973. Gravity, bathymetry and convection in the earth. Earth and Planetary Science Letters 18. doi:10.1016/0012-821X(73)90095-2.

Beaumont, C., Jamieson, R., Nguyen, M., Lee, B., 2001. Himalayan tectonics explained by extrusion of a low-viscosity crustal channel coupled to focused surface denudation. Nature 414, 738–742. doi:10.1038/414738a.

Braun, J., 2006. Recent advances and current problems in modelling surface processes and their interaction with crustal deformation. Geological Society, London, Special Publications 253, 307–325.

Braun, J., 2010. The many surface expressions of mantle dynamics. Nature Geosci 3, 825–833.

Crameri, F., Schmeling, H., Golabek, G.J., Duretz, T., Orendt, R., Buiter, S.J.H., May, D.A., Kaus, B.J.P., Gerya, T.V., Tackley, P.J., 2012. A comparison of numerical surface topography calculations in geodynamic modelling: an evaluation of the sticky air method. Geophysical Journal International 189. doi:10.1111/j.1365-246X.2012.05388.x.

Crouzeix, M., Raviart, P.A., 1973. Conforming and nonconforming finite element methods for solving the stationary stokes equations I. Reveu française d'automatique, informatique, recherche opérationnelle. Mathématique tome 7, 33–75.

Dabrowski, M., Krotkiewski, M., Schmid, D.W., 2008. Milamin: Matlab-based finite element method solver for large problems. Geochemistry, Geophysics, Geosystems 9.

De Bremaecker, J., 1976. Relief and gravity anomalies over a convecting mantle. Geophysical Journal International 45, 349–356. doi:10.1111/j.1365-246X.1976.tb00330.x.

Duretz, T., May, D.A., Gerya, T.V., Tackley, P.J., 2011. Discretization errors and free surface stabilization in the finite difference and marker-in-cell method for applied geodynamics: A numerical study. Geochemistry, Geophysics, Geosystems 12, n/a–n/a. doi:10.1029/2011GC003567.

Finnegan, N.J., Hallet, B., Montgomery, D.R., Zeitler, P.K., Stone, J.O., Anders, A.M., Yuping, L., 2008. Coupling of rock uplift and river incision in the namche Barwa-Gyala peri massif, tibet. Geological Society of America Bulletin 120. doi:10.1130/B26224.1.

Fleitout, L., Froidevaux, C., Yuen, D., 1986. Active lithospheric thinning. Tectonophysics 132. doi:10.1016/0040-1951(86)90037-5.

Gerya, T.V., Yuen, D.A., 2003. Rayleightaylor instabilities from hydration and melting propel cold plumes at subduction zones. Earth and Planetary Science Letters 212, 47 – 62. doi:http://dx.doi.org/10.1016/S0012-821X(03)00265-6.

Hager, B.H., Clayton, R.W., Richards, M.A., Comer, R.P., Dziewonski, A.M., 1985. Lower mantle heterogeneity, dynamic topography and the geoid. Nature 313, 541–545.

Harlow, F., Shannon, J., Welch, J., 1965. Liquid waves by computer. Science (New York, N.Y.) 149, 1092–1093. doi:10.1126/science.149.3688.1092.

Hughes, T.J.R., 2000. The finite element method : linear static and dynamic finite element analysis. Dover Publications, Mineola, NY. ID: 301049178.

Kaus, B.J., Mühlhaus, H., May, D.A., 2010. A stabilization algorithm for geodynamic numerical simulations with a free surface. Physics of the Earth and Planetary Interiors 181. doi:10.1016/j.pepi.2010.04.007.

Koons, P.O., 2002. Mechanical links between erosion and metamorphism in nanga parbat, pakistan himalaya. American Journal of Science 302. doi:10.2475/ajs.302.9.749.

Kramer, S.C., Wilson, C.R., Davies, D.R., 2012. An implicit free surface algorithm for geodynamical simulations. Physics of the Earth and Planetary Interiors 194195, 25 – 37. doi:http://dx.doi.org/10.1016/j.pepi.2012.01.001.

McKenzie, D., 1977. Surface deformation, gravity anomalies and convection. Geophysical Journal of the Royal Astronomical Society 48, 211–238.

Melosh, H.J., Raefsky, A., 1980. The dynamical origin of subduction zone topography. Geophysical Journal of the Royal Astronomical Society 60, 333–354.

Poliakov, A., Podladchikov, Y., 1992. Diapirism and topography. Geophysical Journal International 109. doi:10.1111/j.1365-246X.1992.tb00117.x.

Popov, A., Sobolev, S., 2008. SLIM3D: a tool for three-dimensional thermomechanical modeling of lithospheric deformation with elasto-visco-plastic rheology. Physics of the Earth and Planetary Interiors 171. URL: http://dx.doi.org/10.1016/j.pepi.2008.03.007, doi:10.1016/j.pepi.2008.03.007.

Ruddiman, W.F., Kutzbach, J.E., 1989. Forcing of late cenozoic northern hemisphere climate by plateau uplift in southern asia and the american west. Journal of Geophysical Research 94. doi:10.1029/JD094iD15p18409.

Shewchuk, J., 1996. Triangle: Engineering a 2d quality mesh generator and delaunay triangulator, in: Lin, M., Manocha, D. (Eds.), Applied Computational Geometry Towards Geometric Engineering. Springer Berlin Heidelberg. volume 1148 of *Lecture Notes in Computer Science*, pp. 203–222. URL: http://dx.doi.org/10.1007/BFb0014497, doi:10.1007/BFb0014497.

Turcotte, D., Schubert, G., 1982. Geodynamics. John Wiley & Sons.

Warzee, G., 1974. Finite element analysis of transient heat conduction application of the weighted residual process. Computer Methods in Applied Mechanics and Engineering 3. doi:10.1016/0045-7825(74)90028-0.

Willett, S.D., 1999. Orogeny and orography: The effects of erosion on the structure of mountain belts. Journal of Geophysical Research 104. doi:10.1029/1999JB900248.

Zaleski, S., Julien, P., 1990. Numerical simulation of salt diapir formation in small and extended geometries. Report, Total-Compagnie Francaise des Petroles .

Zhong, S., Gurnis, M., Hulbert, G., 1993. Accurate determination of surface normal stress in viscous flow from a consistent boundary flux method. Physics of the Earth and Planetary Interiors 78, 1–8.

Zhong, S., Gurnis, M., Moresi, L., 1996. Free-surface formulation of mantle convection-i, basic theory and application to plumes. Geophysical Journal International 127, 708–718.

Zienkiewicz, O., Vilotte, J., Toyoshima, S., 1985. Iterative method for constrained and mixed approximation. an inexpensive improvement of FEM performance .

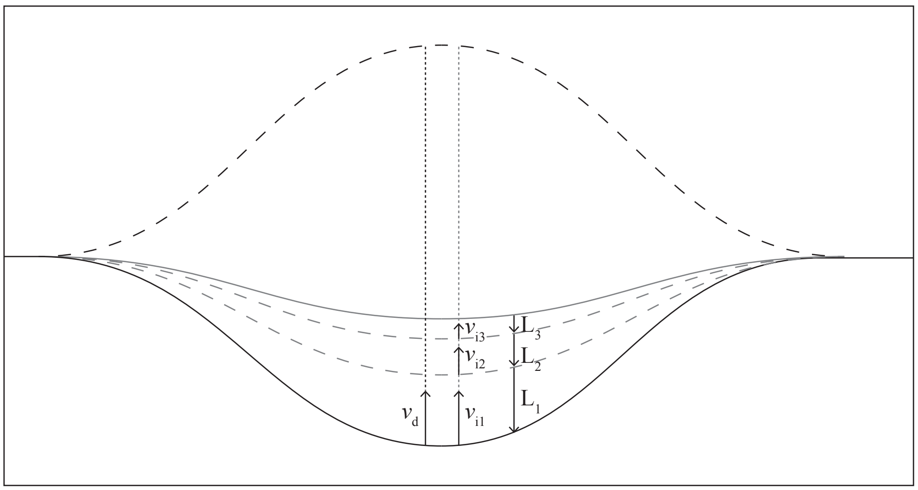

Figure 1: Evolution of a valley-shape negative topography with different time steps. The solid black line represents the initial negative topography (mass defect). Theoretically, the negative topography should rise into a flat line due to buoyancy. Lets consider now two cases: 1) a single big time step (TS) for which the calculated velocity is v_d, where the dashed black line represents the positive unstable topography for the next time step, calculated with v_d; and 2) smaller time steps ts_1, ts_2, and ts_3, such as $TS = ts_1 + ts_2 + ts_3$, with respective calculated velocities v_{i1}, v_{i2} and v_{i3}, and load increments L_1, L_2 and L_3, the dashed grey lines represent smoother negative topographies at the end of the time steps ts_1 and ts_2, and the solid grey line represents a more realistic and stable topography at the end of ts_3, equivalent in time to the unstable topography of the case 1. For the case 1, the load increments are not considered into the body forces, so the resulting integrated displacement is bigger than the integrated displacement through the small time steps, for which body forces are updated with the load increments at the beginning of each ts. The instability of the free surface is the consequence of a time step bigger than the viscous relaxation time, which often leads to an overestimation of the velocities at the beginning of the next time step.

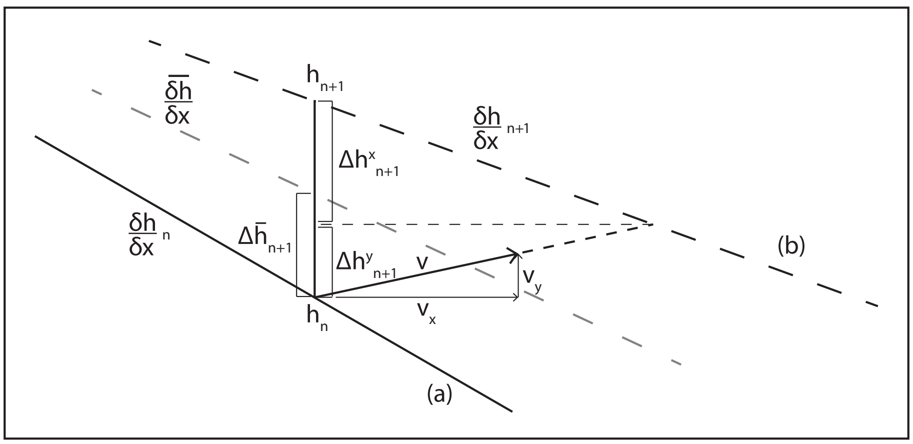

Figure 2: Increments in height Δh at a surface node (a) before and (b) after a time step at the same horizontal location: v represents the velocity at the beginning of the time step, h_n and h_{n+1} are the height at the beginning and end of the time step respectively, Δh^x_{n+1} and Δh^y_{n+1} are the height increments after the time step, calculated using v_x and v_y components of the velocity respectively, $\left(\frac{\delta h}{\delta x}\right)_n$, $\left(\frac{\delta h}{\delta x}\right)_{n+1}$ and $\left(\frac{\bar{\delta h}}{\delta x}\right)$ are the surface slopes at the beginning, at the end, and an average approximation during of the time step respectively, and $\Delta\bar{h}_n$ is the portion of the height increment for the end of the time step, obtained for a given choice of the α and β controlling factors.

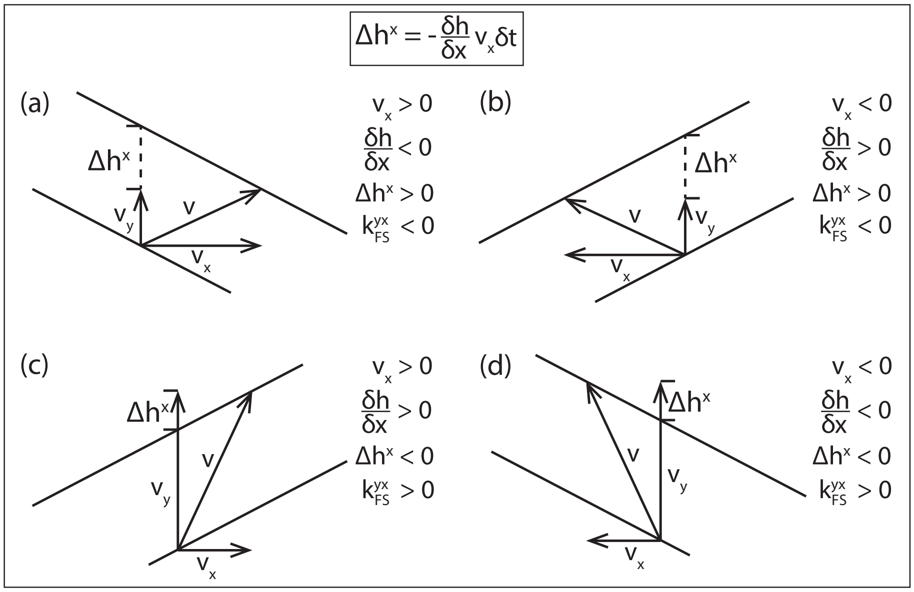

Figure 3: Different configurations of positive vertical velocities v_y with positive and negative horizontal velocities v_x and positive and negative slopes $\frac{\delta h}{\delta x}$: (a) and (b) horizontal velocities v_x result in positive vertical displacements of the surface Δh^x, for the given slopes that should be penalized with a negative k_{FS}^{yx} term, while (c) and (d) horizontal velocities v_x for the given slopes result in negative displacements of the surface Δh^x that should be penalized with a positive k_{FS}^{yx}. Note that the term k_{FS}^{yx} is opposite in sign to the displacement Δh^x. This change in sign is due to the negative sign of the gravity.

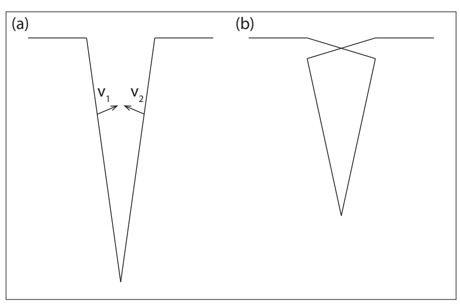

Figure 4: Self-intersection of surface topography created by a surface valley with very steep slopes. In this case the surface velocities v_1 and v_2 in (a) induce large horizontal displacements during a time step leading to a numerical artefact in which the top-surface intersects itself after a Lagrangian time step as shown in (b).

Table 1: Experiment parameters

Test	Viscosity η [Pa s]	Geometry parameters [Km]	Geometry
Decaying-half-sinusoid of top-surface relief	10^{21}	500x500 A = 10	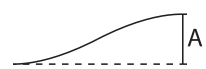
Multiple harmonics of top-surface relief	10^{21}	500x500 A = 10 $\lambda = 10$	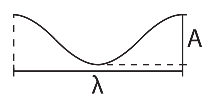
Rayleigh-Taylor instability beneath a free top surface	$\eta_1 = 10^{21}$ $\eta_2 = 10^{20}$	500x500 A = 10	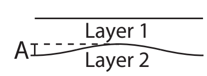
Steep-slope along a free top surface	10^{21}	5x0.1 A = 2 $\Theta = 30°$	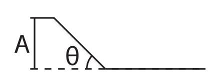

Table 2: Topographical RMS differences between tests with different small δt and α, after 1 Myr. Note that the differences are smaller than the ones shown in figure 7, that compares larger time steps with a reference of $\delta t = 100$ yr and $\alpha = 0$.

Small δt comparisons	$(\delta t_{100}\alpha_0 - \delta t_{100}\alpha_{0.5})$ [m]	$(\delta t_{200}\alpha_0 - \delta t_{100}\alpha_0)$ [m]	$(\delta t_{200}\alpha_{0.5} - \delta t_{100}\alpha_{0.5})$ [m]
Decaying-half-sinusoid relief	7.196×10^{-3}	7.195×10^{-3}	5.746×10^{-7}
50th-harmonic-sinusoidal relief	8.595×10^{-2}	1.133×10^{-1}	7.503×10^{-2}
Rayleigh-Taylor instability	5.040×10^{-3}	4.177×10^{-4}	9.159×10^{-3}
Steep-slope	3.198×10^{-3}	3.241×10^{-3}	1.927×10^{-3}

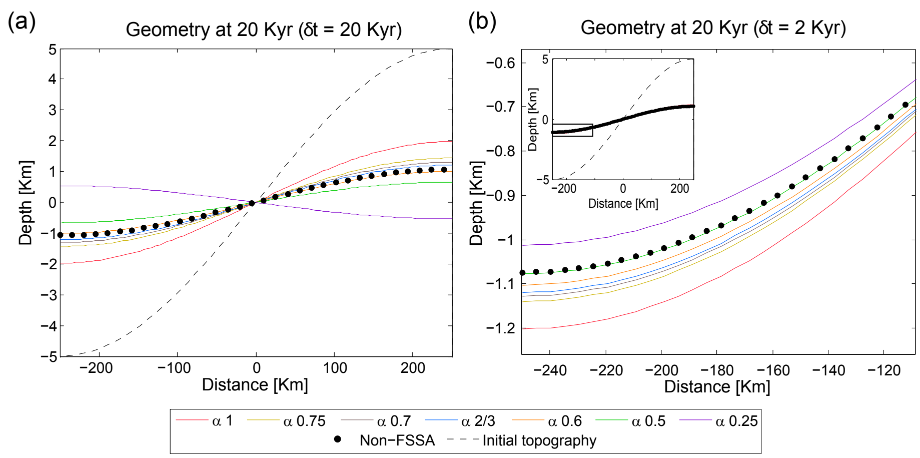

Figure 5: Topographies generated after 20 Kyr, calculated with (a) a time step of 20 Kyr and (b) a time step of 2 Kyr for different α, with $\beta = 1$. (a) The topographies generated for different choices of α after the first 20 Kyr time step show remarkable differences from one to another; $\alpha = 0.25$ leads to instability since the topography is inverted after a single step, with $\alpha = 0.6$ and $2/3$ calculations yield the most accurate results. $\alpha = 0.6$ is more likely than higher values to trigger instability in future steps, since it results into an small overestimate of the surface displacement. (b) The topographies generated with the more stable FSSA approximation and a ten-fold smaller time step differ by less than 200 m from one to another. The most accurate results for small time-steps are obtained with $\alpha = 0.5$.

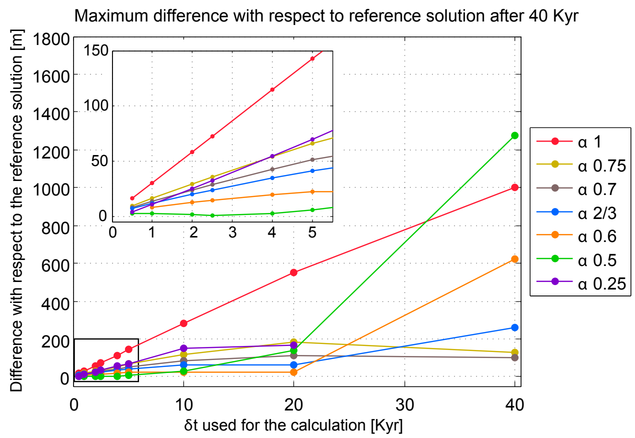

Figure 6: Maximum absolute differences between the topography calculated for FSSA approximations with different α and δt, and the topography calculated with a very small $\delta t = 100$ yr using no FSSA. $\alpha = 0.5$ is most accurate for smaller time steps where the method is numerically stabler, while $\alpha = 0.7$, $2/3$ and 0.6 are more accurate for larger time steps that result numerical instabilities in experiments without FSSA stabilization ($\delta t > 14$ Kyr).

Table 3: Stability tests. δt represents the time step from which the different tests start to be unstable or having mesh problems, t_b is the run time for which the tests break, and the capital letters indicate the way the tests fail, where DS stands for 'drunken sailor' instability, SIS for the self-intersecting surface artefact instability (Fig. 4) and MESH for an artefact in which inner nodes become displaced outside of the border of the evolving Lagrangian mesh.

Test	Total run-time interval	Non-FSSA (max δt)	Kaus $\alpha_K = 0.5$	Kaus $\alpha_K = 2/3$	$\alpha = 0.5$ $\beta = 0$	$\alpha = 2/3$ $\beta = 0$	$\alpha = 2/3$ $\beta = 0.5$	$\alpha = 2/3$ $\beta = 1$
Decaying-half-sinusoid relief	5 Myr	DS δt 14 Kyr t_b 14 Kyr	DS δt 27 Kyr t_b 27 Kyr	DS δt 40 Kyr t_b 40 Kyr	DS δt 27 Kyr t_b 27 Kyr	DS δt 40 Kyr t_b 40 Kyr	DS δt 40 Kyr t_b 40 Kyr	DS δt 40 Kyr t_b 40 Kyr
50th-harmonic-sinusoidal relief	20 Myr	DS δt 30 Kyr t_b 1.11 Myr	SIS δt 620 Kyr t_b 19.84 Myr	SIS δt 570 Kyr t_b 18.81 Myr	SIS δt 610 Kyr t_b 19.52 Myr	SIS δt 510 Kyr t_b 18.87 Myr	SIS δt 500 Kyr t_b 19 Myr	SIS δt 500 Kyr t_b 19 Kyr
Rayleigh-Taylor instability	7 Myr	DS δt 5 Kyr t_b 50 Kyr	DS δt 16 Kyr t_b 720 Kyr	DS δt 35 Kyr t_b 525 Kyr	DS δt 16 Kyr t_b 752 Kyr	DS δt 35 Kyr t_b 525 Kyr	DS δt 35 Kyr t_b 525 Kyr	DS δt 35 Kyr t_b 525 Kyr
Steep-slope	100 Myr	MESH δt 2.7 Myr t_b 5.4 Myr	MESH δt 4.7 Myr t_b 9.4 Myr	MESH δt 5.6 Myr t_b 11.2 Myr	MESH δt 4.7 Myr t_b 9.4 Myr	MESH δt 5.6 Myr t_b 11.2 Myr	MESH δt 5.9 Myr t_b 11.8 Myr	SIS δt 4.3 Myr t_b 12.9 Myr

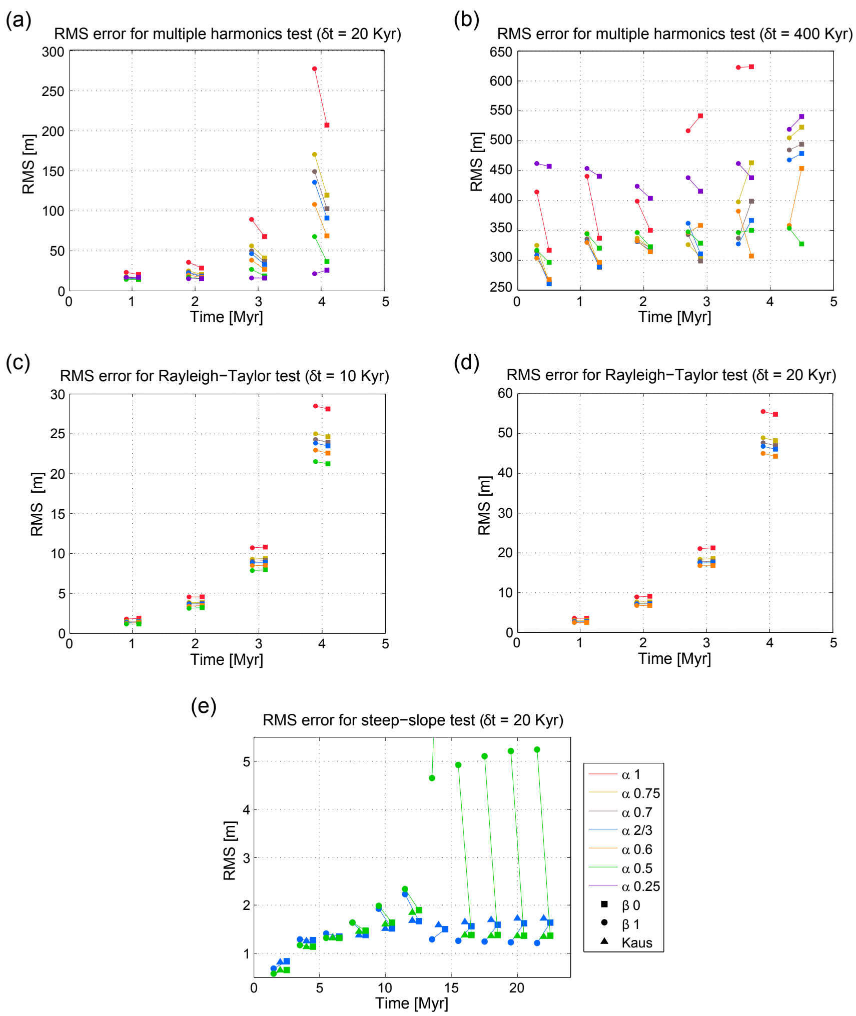

Figure 7: Root-mean-square errors obtained from the difference between the topographies calculated with FSSAs for various α and β, and the non-FSSA reference solution calculated using $\delta t = 100$ yr for: (a) and (b) decaying 50th-harmonic sinusoidal relief for $\delta t = 20$ and 400 Kyr respectively, (c) and (d) the Rayleigh-Taylor instability test for $\delta t = 10$ and 20 Kyr respectively, and (e) the steep-slope test for $\delta t = 20$ Kyr. RMS differences for $\alpha = 0.25$ for (c) and $\alpha = 0.25$ and 0.5 for (d) are not plotted because these tests result in an unstable numerical solution.

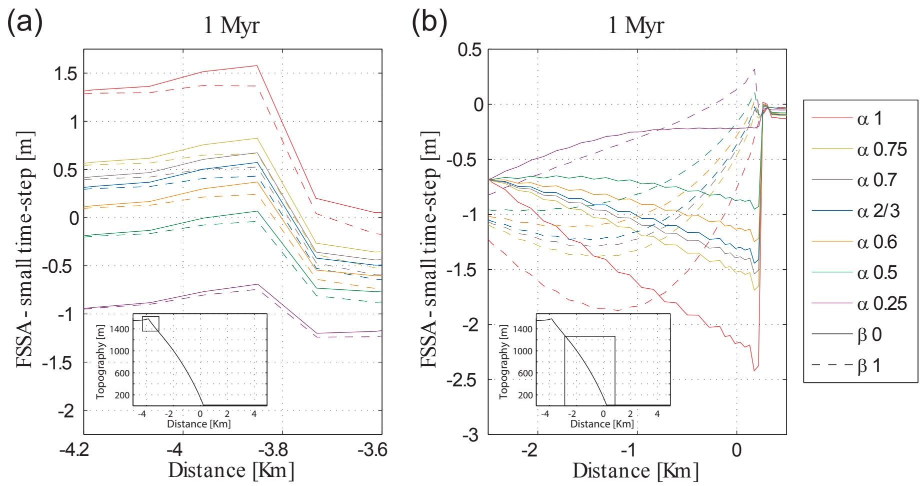

Figure 8: Steep-slope relief differences between topographies calculated with FSSA methods using different α and β parameters and $\delta t = 20$ Kyr and a reference non-FSSA solution with a 100 yr time step during a 1 Myr time run. Note that for the upper topographic inflexion (a) the tests $\alpha = 0.5$, 0.6 and 2/3, and $\beta = 0$ and 1 are more accurate. Note also that $\beta = 1$ tests for any α results in more accurate topographies at the end of the slope (b), where the horizontal velocities are bigger.